Tomographic Reconstruction of Two-Dimensional Residual Strain Fields from Bragg-Edge Neutron Imaging

A.W.T. Gregg,[1,*] J.N. Hendriks,[1] C.M. Wensrich,[1] A. Wills,[1] A.S. Tremsin,[2] V. Luzin,[3] T. Shinohara,[4] O. Kirstein,[1,5] M.H. Meylan,[6] and E.H. Kisi[1]

[1] *School of Engineering, The University of Newcastle, Callaghan, New South Wales 2308, Australia*
[2] *Space Sciences Laboratory, University of California, Berkeley, California 94720, USA*
[3] *Australian Centre for Neutron Scattering, Australian Nuclear Science and Technology Organisation, Kirrawee, New South Wales 2232, Australia*
[4] *Materials and Life Sciences Facility, Japan Proton Accelerator Research Complex, Tokai-mura, Ibaraki 319-1195, Japan*
[5] *European Spallation Source, Lund SE-223 63, Sweden*
[6] *School of Mathematical and Physical Sciences, The University of Newcastle, Callaghan, New South Wales 2308, Australia*

(Received 15 February 2018; revised manuscript received 6 August 2018; published 13 December 2018)

Bragg-edge strain imaging from energy-resolved neutron-transmission measurements poses an interesting tomography problem. The solution to this problem will allow the reconstruction of detailed triaxial stress and strain distributions within polycrystalline solids from sets of Bragg-edge strain images. Work over the last decade has provided some solutions for a limited number of special cases. In this paper we provide a general approach to reconstruction of an arbitrary system based on a least-squares process constrained by equilibrium. This approach is developed in two dimensions before it is demonstrated experimentally on two samples with use of the RADEN instrument at the Japan Proton Accelerator Research Complex spallation neutron source. Validation of the resulting reconstructions is provided through a comparison with conventional constant-wavelength strain measurements performed with the KOWARI engineering diffractometer of the Australian Nuclear Science and Technology Organisation. The paper concludes with a discussion on the range of problems to be addressed in a three-dimensional implementation.

DOI: 10.1103/PhysRevApplied.10.064034

I. INTRODUCTION

Energy-resolved neutron-transmission techniques now provide a means for obtaining high-resolution images of strain within polycrystalline solids [1–4]. These techniques rely on relative shifts of abrupt changes in the transmission rate as a function of wavelength—known as "Bragg edges"—the positions of which are governed by diffraction; at the point where Bragg's law can no longer be fulfilled for a given set of lattice planes, the transmitted intensity abruptly rises.

Detailed descriptions of this approach can be found elsewhere (e.g., Refs. [1,5]). Briefly, the process involves the measurement of thermal transmission-spectra, typically with use of time-of-flight techniques at pulsed neutron sources [e.g., the Japan Proton Accelerator Research Complex (J-PARC) in Japan, ISIS in the United Kingdom, or the Spallation Neutron Source in the USA]. Current detector technology is now able to perform such measurements simultaneously over arrays of individual pixels as small as 55 μm. From these data, shifts in the position of observed Bragg edges relative to a reference stress-free sample provide a measure of strain.

The salient points of such a measurement can be summarized as follows:

(1) As with all diffraction-based techniques, strain measured in this way represents the elastic component alone.
(2) The measured strain is the normal component in the transmission direction of the neutron beam.
(3) Strain measured by each detector pixel represents a through-thickness average along the path of the corresponding ray.

The success of this approach and development of instruments and associated detector technologies has prompted activity focused on solving the associated tomographic reconstruction problem [6–13]. The aim is to provide a

*alexander.gregg@newcastle.edu.au

method analogous to conventional computed tomography (CT) by which the full triaxial strain distribution within a sample could be reconstructed from a sufficient set of Bragg-edge strain images. This involves the reconstruction of a tensor field, an inherently more complex task than conventional scalar CT.

Once developed, this approach has the potential to make a significant impact in a number of areas in experimental mechanics. A prominent example concerns the assessment of residual stress fields in systems such as additively manufactured, laser-clad, peened, welded, cast, forged, and/or otherwise-processed components. In each case, residual stress locked in by the manufacturing process has a critical impact on the strength and performance of the resulting parts. Bragg-edge strain tomography promises a unique full-field approach to examining these systems over practical length scales.

This task revolves around the inversion of the longitudinal ray transform (LRT), which represents an appropriate model of the measurement process [9]. While, in general, this is a three-dimensional problem, for simplicity we consider only two dimensions in this paper.

With reference to the coordinate system and geometry shown in Fig. 1, the LRT can be written as

$$\Gamma_\epsilon(p,\theta) = \frac{1}{L}\int_0^L \epsilon_{ij}\,(x(s,p), y(s,p))\hat{n}_i\hat{n}_j\, ds,$$

where the rank-2-tensor strain field $\boldsymbol{\epsilon}$ is mapped to the average normal component of strain, Γ_ϵ, along the ray with direction $\hat{\boldsymbol{n}} = [\cos\theta, \sin\theta]^T$ arriving at position p on the detector.

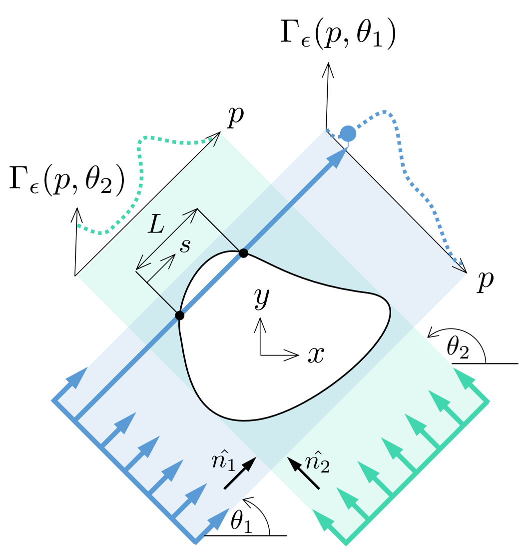

FIG. 1. A single ray passes through a sample and provides a measurement of the through-thickness average normal strain in the direction of the ray at a detector pixel. For each projection angle, θ, measurements across the detector form a profile $\Gamma_\epsilon(p,\theta)$.

From Lionheart and Withers [9], the LRT is known to be a non-injective mapping (from $\boldsymbol{\epsilon}(x,y)$ to $\Gamma_\epsilon(p,\theta)$). Strain fields producing any given set of projections are not unique. As a consequence, general tomographic reconstruction is not possible from the measurements alone; additional information or constraints are required to isolate the correct (i.e., physical) field from all the possibilities. To this end, a number of approaches have been developed that rely on assumptions of compatibility or equilibrium to further constrain the problem.

Compatible strain fields are those that can be written as the gradient of a displacement field in a simply connected body (i.e., conservative). In general, this is always the case. However, when the total strain has both elastic and inelastic parts, only the compatibility of the sum is guaranteed. If compatibility of the *elastic* component can be assumed (e.g., in the absence of plasticity or other forms of eigenstrain), a strong constraint on the reconstruction problem exists. This constraint was central to the success of a number of prior reconstruction algorithms.

For example, the seminal work by Abbey *et al.* [6,7] on axisymmetric systems examined the reconstruction of strain within quenched cylinders and a standard Versailles Project on Advanced Materials and Standards (VAMAS) ring-and-plug sample using various basis functions alongside assumptions of compatibility. Outside axisymmetric systems, reconstructions have been demonstrated for a number of special cases; for example, granular systems [10], and strain fields resulting from *in situ* loads [11,12], where elastic strain compatibility can be assumed.

Unfortunately, in the vast majority of residual stress problems (e.g., all of the examples mentioned earlier), the elastic component of strain is inherently incompatible. While compatibility cannot generally be assumed, equilibrium must always be satisfied. Two separate algorithms for axisymmetric systems have been presented that rely on this assumption [8,13].

In the case of Kirkwood *et al.* [8], the assumption of equilibrium was not apparent at the time; it was a consequence of their approach to boundary conditions. In contrast, equilibrium was explicit and central to the method presented in Ref. [13]. Equilibrium is also central to the method presented in Ref. [14], where the unknown strain is reconstructed by a machine-learning technique known as a "Gaussian process" [15]. This probabilistic method approaches the problem by considering strain as a distribution of Airy stress functions, which automatically satisfy equilibrium.

In this paper we develop an approach for reconstruction of arbitrary two-dimensional systems using an equilibrium constraint to provide unique solutions. The resulting algorithm is demonstrated both in simulation and on experimental data. We also provide a brief discussion on the potential extension to three dimensions.

II. APPROACH

The typical geometry for Bragg-edge strain imaging is shown in Fig. 1. In each orientation, θ_i, a profile of the form $\Gamma_\epsilon(p,\theta_i)$ is measured across the width of the detector—each detector pixel contributes one point to this profile. Inherent symmetry of the transform implies projections over 180° are sufficient; however, in practice measurements are usually taken over an entire revolution. A complete set of profiles can be arranged to form a transformed image that resembles a traditional sinogram (see, e.g., Fig. 3). Given this *strain sinogram*, we seek to recover $\boldsymbol{\epsilon}$ from the infinite number of fields that potentially map to it.

Our approach is as follows:

(1) Define a basis for the set of possible strain fields, $\mathcal{E}$. Elements of $\mathcal{E}$ may not necessarily be physical (i.e., they may not satisfy equilibrium).

(2) Compute the corresponding set of strain sinograms, $\mathcal{S}$, by mapping each element of $\mathcal{E}$ through the LRT. This forward projection involves numerical integration along ray paths.

(3) Through constrained least-squares fitting, find a linear combination from $\mathcal{E}$ such that

(a) The corresponding combination from $\mathcal{S}$ provides the measured strain sinogram.

(b) Equilibrium is satisfied at a sufficient number of test points.

In a numerical implementation, $\mathcal{E}$ is composed of a finite number of elements. Ideally this set should be orthogonal and ordered with increasing complexity to facilitate truncation. To this end, our approach uses a two-dimensional Fourier basis to write each component of strain in the form

$$\begin{aligned}\epsilon_{ij}(x,y) = \sum_{a,b\in\mathbb{Z}} &\alpha_{ij}^{a,b}\sin\left(\frac{a\pi}{L}x\right)\sin\left(\frac{b\pi}{W}y\right)\\ &+\beta_{ij}^{a,b}\sin\left(\frac{a\pi}{L}x\right)\cos\left(\frac{b\pi}{W}y\right)\\ &+\gamma_{ij}^{a,b}\cos\left(\frac{a\pi}{L}x\right)\sin\left(\frac{b\pi}{W}y\right)\\ &+\eta_{ij}^{a,b}\cos\left(\frac{a\pi}{L}x\right)\cos\left(\frac{b\pi}{W}y\right),\end{aligned}$$

where a and b are wave numbers, L and W are characteristic dimensions of the geometry, and $\alpha_{ij}^{a,b}\ldots\eta_{ij}^{a,b}$ are unknown coefficients to be determined by the algorithm.

Truncation of this basis to n and m wave numbers in the x and y directions, respectively (i.e., $a\in[0,n]$, $b\in[0,m]$), gives $12nm+3$ tensor functions—four sinusoids for each component of strain, three components for each permutation of wave numbers, and three constant fields. While the forward mapping of these functions is potentially a large task, it can be done off-line and ahead of time. In other words, a library of basis pairs can be calculated before any experiment provided that the sample geometry is known.

Through Hooke's law, the equations of equilibrium can be written directly in terms of strain. In two dimensions, this relies on either a plane-stress or a plane-strain assumption. For example, assuming plane stress, we have

$$\begin{aligned}\frac{\partial}{\partial x}(\epsilon_{xx}+\nu\epsilon_{yy})+\frac{\partial}{\partial y}(1-\nu)\epsilon_{xy}=0,\\ \frac{\partial}{\partial y}(\epsilon_{yy}+\nu\epsilon_{xx})+\frac{\partial}{\partial x}(1-\nu)\epsilon_{xy}=0,\end{aligned}$$

where ν is Poisson's ratio.

Our algorithm imposes these two equations at a set of test points distributed over the interior of the sample. At each point this provides a linear constraint on the unknown coefficients.

The resulting constrained least-squares problem can be solved by a variety of techniques. Our algorithm uses the `lsqlin` MATLAB intrinsic function.

The choice of n and m requires no *a priori* knowledge of the system; the size of the basis can be chosen as the minimum required to capture the relevant features in the observed strain sinogram. This can be assessed by examination of the residual between the strain sinogram and the fitted version; ideally no structure should be visible above random noise. In a sense, in terms of the resulting reconstruction, n and m have some similarity to resolution; however, they are certainly not the same.

III. DEMONSTRATION: SIMULATION

We first demonstrate this algorithm on the classical cantilevered beam as examined by Wensrich *et al.* [11] and shown in Fig. 2. Under a plane-stress assumption, the Saint-Venant approximation to the resulting strain field is [16]

$$\boldsymbol{\epsilon}(x,y)=\begin{bmatrix}\frac{P}{EI}(\ell-x)y & -\frac{(1+\nu)P}{2EI}\left[\left(\frac{w}{2}\right)^2-y^2\right]\\ -\frac{(1+\nu)P}{2EI}\left[\left(\frac{w}{2}\right)^2-y^2\right] & -\frac{\nu P}{EI}(\ell-x)y\end{bmatrix},$$

where I is the second moment of area, P is the applied load, E is Young's modulus, ν is Poisson's ratio, and ℓ and w are the dimensions shown in Fig. 2.

Note that this strain field is compatible, a fact that was central to the previous approach. In contrast, no such assumption is made by the current algorithm.

Fifty Bragg-edge strain profiles over equally spaced angles between 0° and 180° are numerically simulated from this field under the assumption of the use of a state-of-the-art microchannel plate detector with 512 pixels over 28

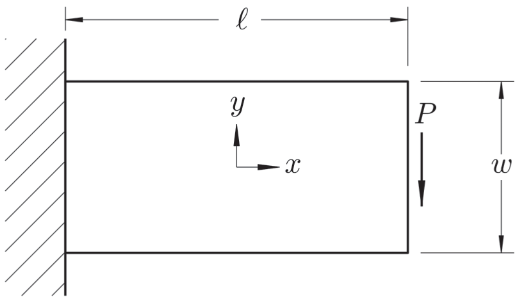

FIG. 2. Cantilevered-beam coordinate system and geometry. $\ell = 20$ mm, $w = 10$ mm, $P = 2$ kN, $E = 200$ GPa, and $\nu = 0.3$ [11].

mm [2]. Gaussian measurement noise with standard deviation $\sigma = 1.25 \times 10^{-4}$ is introduced, a value within the capabilities of current neutron instruments [12].

The simulated strain sinogram, the resulting fit from $\mathcal{S}$, and its residual based on $n = m = 8$ wave numbers and a mesh of 1000 equally spaced equilibrium test points are shown in Fig. 3. Characteristic lengths are chosen from the sample dimensions ($L = \ell$, $W = w$). It is clear that the residual has no structure, implying that a sufficient number of basis vectors have been used.

The resulting reconstruction in Fig. 4 shows close agreement with the physical solution. Overall, the absolute error in strain is below 2.7×10^{-5}, almost 1 order of magnitude below the noise introduced into the measurements. This indicates that the mesh of equilibrium test points is sufficiently dense to isolate the physical solution. Note that increasing the number of equilibrium points does not add significant computational burden; in most cases the additional constraints aid the convergence.

Direct comparison with the algorithm described by Wensrich *et al.* [11] shows significantly faster convergence for this system (see Fig. 5). As expected, as the order of the basis increases, the convergence is slower; however, even at $n = m = 10$ the convergence is at least twice as fast. With $n = m = 10$, our problem involves 1203 unknown coefficients, far in excess of the 242 unknown boundary displacements in Ref. [11].

IV. DEMONSTRATION: EXPERIMENTAL

Following success in simulation, the algorithm is demonstrated on real-world examples in an experiment with the RADEN energy-resolved-neutron-imaging instrument at J-PARC [17,18]. This experiment focuses on reconstructing residual strain fields within two EN26 steel samples (medium carbon, low alloy) as follows:

(1) A crushed ring formed through plastically deforming a hollow cylinder.

(2) An offset ring-and-plug system with residual strain resulting from an interference (i.e., shrink) fit.

These samples are specifically designed to test the algorithm in the case of both continuous (crushed-ring) and discontinuous (ring-and-plug) strain fields.

Each sample is manufactured from the same bar of EN26 steel and is heat treated with an identical process to relieve stress and provide a uniform tempered-martensite structure (i.e., ferritic) before crushing or assembly. Both samples have a final hardness of 290 HV and are 14 m tall. Sample geometries are shown in Fig. 6.

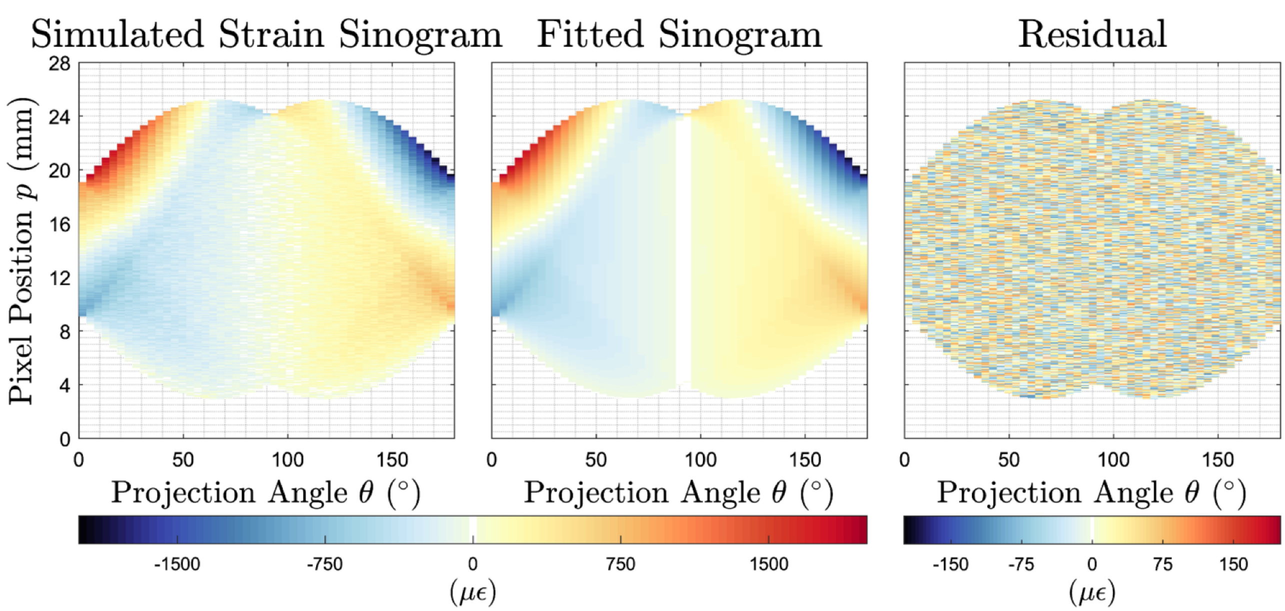

FIG. 3. A simulated strain sinogram from the cantilevered beam shown in Fig. 2, the fitted strain-sinogram obtained with eight wave numbers in the x and y directions, and spatial residual in the fit.

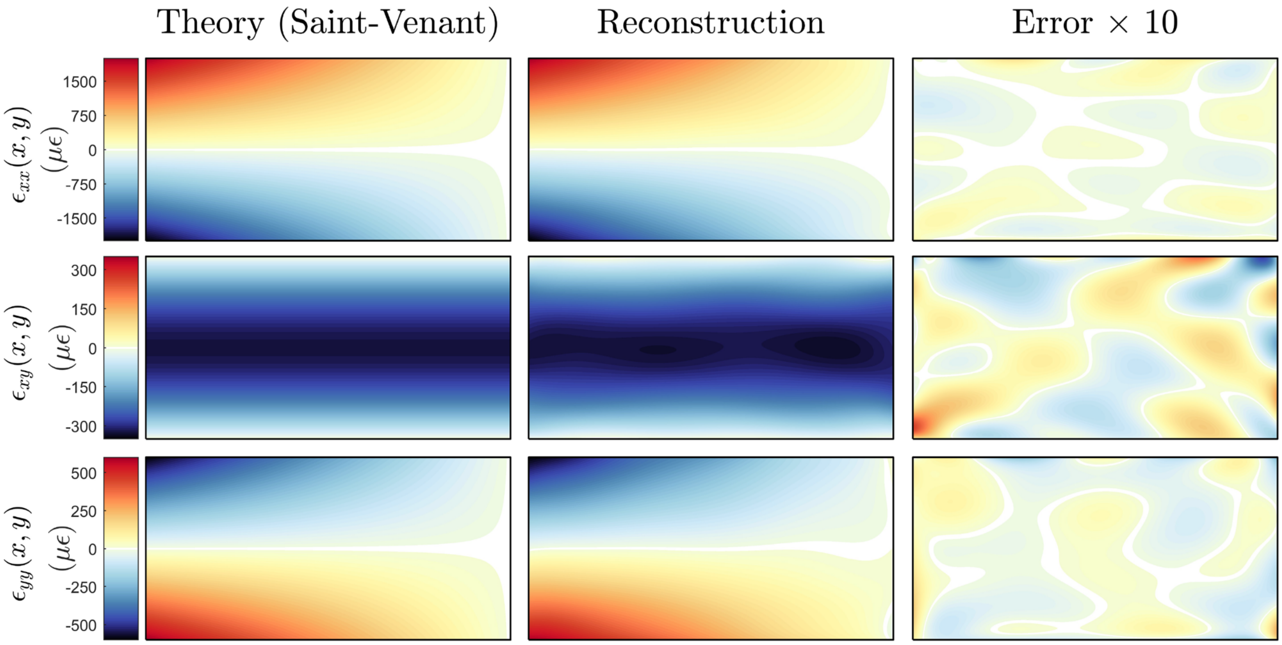

FIG. 4. The Saint-Venant solution from which measurements are simulated, the reconstructed strain field, and the error, scaled by a factor of 10.

The first sample is plastically deformed by 1.5 mm on the diameter with approximately 8.4 kN of load from hardened steel platens in a mechanical testing machine.

The second sample contains a total interference of 40 ± 2 μm produced through cylindrical grinding. Finite-element simulation suggested that this would provide strains of significant magnitude below yield. After manufacture, the sample is assembled through a shrink-fit process (380 °C versus −196 °C).

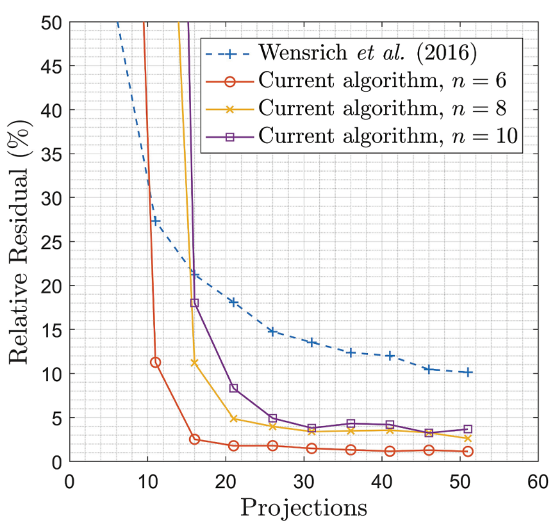

FIG. 5. Convergence of the algorithm for the cantilevered beam as compared with the boundary reconstruction method presented in Wensrich *et al.* [11].

Strain profiles are measured from both samples simultaneously on the RADEN instrument together with a microchannel plate detector (512 × 512 pixels, 55 μm per pixel) at a distance of 17.9 m from the source. The source power is 409 kW (January 2018). Counts are binned into half-columns corresponding to the full height of each sample (one pixel wide) to provide the measured profiles $\Gamma_\epsilon(p,\theta)$ as shown in Fig. 7. The resolution of the profiles is estimated from the sharpness of the sample boundaries and is found to be approximately 100 μm. This does not correspond to the resolution of the final reconstructions, which, as mentioned earlier, is a more complicated matter.

Each individual strain measurement is of the form

$$\bar{\epsilon} = \frac{d - d_0}{d_0},$$

where the atomic lattice spacing d is found through fitting the integral form of the Kropff model to the (110) Bragg edge, with d_0 the undeformed reference spacing (assumed

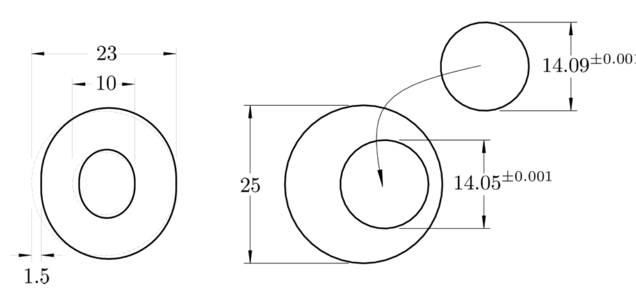

FIG. 6. Sample geometries: the crushed ring and the offset ring and plug. All dimensions are in millimeters.

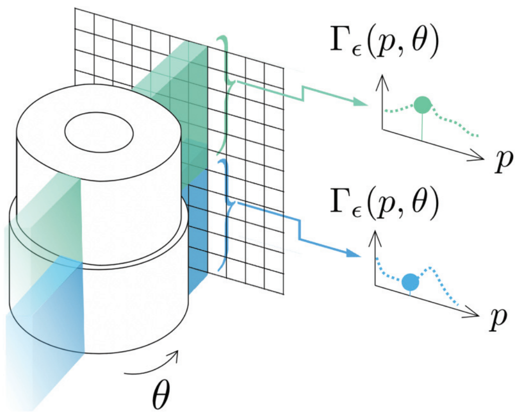

FIG. 7. Neutron counts are binned over half-columns of pixels to provide a profile $\Gamma_\epsilon(p,\theta)$ from each sample.

constant). A typical edge fit is shown in Fig. 8. A more-detailed description of the fitting process is outlined in Refs. [1,2].

Throughout the experiment it is apparent that the fitted edge position is sensitive to sample thickness. This effect was previously described by Vogel [19]; however, the exact mechanism is yet to be established. Potentially, the effect is a consequence of a weighting toward shorter wavelengths in the transmission spectrum with sample thickness due to energy-dependent attenuation—generally known as "beam hardening" [20]. In our case, this may lead to a systematic bias in the observed location of edges depending on the path length. Along with a decrease in the height, beam hardening can slightly modify the shape of an edge, and sensitivity between parameters in the curve-fitting process can result in a perceived pseudostrain.

To account for this effect, a correction is applied to d_0 as determined via a stress-relieved wedge-shaped sample.

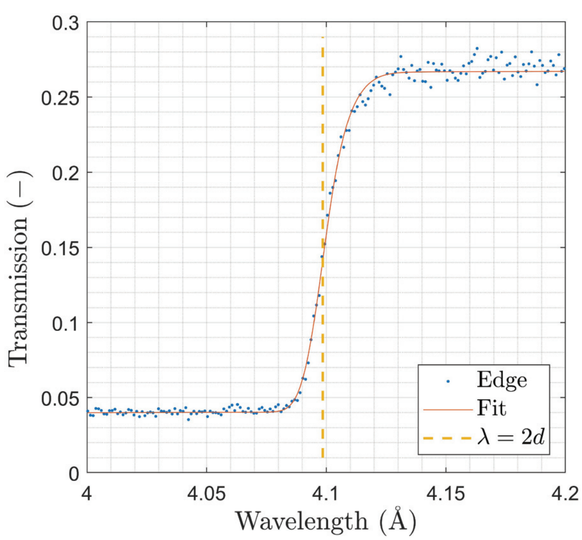

FIG. 8. A typical measurement of the (110) Bragg edge together with a fitted profile based on the Kropff model.

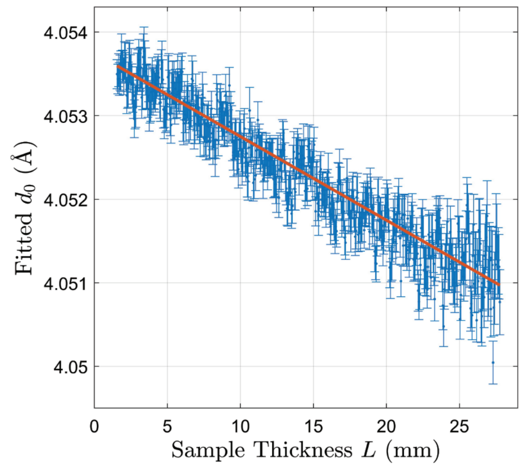

FIG. 9. Bias in the fitted d_0 value as a function of the irradiated path length.

Bragg-edge positions are measured from this sample over 9 h, allowing a linear trend against thickness to be determined as shown in Fig. 9.

This empirical model proved sufficient for our purposes; however, a more theoretical approach based on known neutron cross sections is being investigated. There is also the potential to approach this problem through full-pattern fitting techniques as described in Refs. [21–25]. Developments in this area of research have the potential to resolve many potential issues in the strain-measurement process, such as texture and grain-size effects, as well as this current issue. At present this is not practical in terms of the number of individual measurements and the time required to fit a single pattern; however, this will certainly improve in the future.

In total, 50 profiles are measured at golden-angle increments [26] in θ with a sampling time of 2 h per projection. This provides a statistical uncertainty in strain on the order 1×10^{-4} over most of the measurements. Together with open-beam and d_0 measurement, 4.5 days of beamtime is used.

Alignment of each sample is determined by matching the projected sample outlines to the conventional sinograms. This involves calculation of positions relative to the center of rotation, and, in the case of the crushed ring, the initial angular offset.

Validation relies on comparison with detailed conventional strain scans [27–29] from the KOWARI constant-wavelength strain diffractometer within the Australian Nuclear Science and Technology Organisation (ANSTO) [30–32]. These scans provide measurements of the three in-plane components of strain over a mesh of points within each sample (174 points in the crushed ring and 195 points in the offset ring and plug). These are based on the relative shift of the (211) diffraction peak measured with neutrons of wavelength $\lambda = 1.67$ Å (90° geometry) and a $0.5 \times 0.5 \times 14$ mm^3 gauge volume. The {211} and {110} lattice planes effectively have the same diffraction elastic constants [33].

Sampling times with the KOWARI diffractometer are based on providing uncertainty in strain of around 7×10^{-5}, which requires around 30 h of beamtime per component in the offset ring and plug and 15 h per component in the crushed ring. Together with sample setup and alignment, a total of 6 days of beamtime is required for the two samples.

V. RESULTS

A. Crushed Ring

The measured strain sinogram from the crushed ring is shown on the left-hand-side in Fig. 10. Reconstruction from these data is performed with ten wave numbers in both the x direction and the y direction and 1000 regularly spaced equilibrium test points over a grid on the interior of the sample. Characteristic lengths are chosen in line with the major and minor axes of the crushed ring. The reconstructed strain field is shown on the left in Fig. 11 compared with an interpolation of the KOWARI strain scans. Figure 12 provides a direct comparison along a number of key cross sections.

In general, the reconstruction shows close agreement to the KOWARI measurement in terms of the overall structure of the strain distribution. In particular, the symmetries present within the sample can be observed within the reconstruction even though no such assumption was made. At a detailed level, there are some areas of discrepancy. For example, the ϵ_{xx} component shows more pronounced banding across the width of the sample compared with the KOWARI measurement, and does not capture the full extent of the square-shaped tensile region in the ϵ_{yy} component.

This behavior is not observed in reconstructions based on simulated measurements from the interpolated KOWARI strain maps—even with significant levels of simulated Gaussian noise. This suggests that the issue is not with the particular field or sample geometry but is with systematic errors in the Bragg-edge fitting process. The validity of the plane-stress assumption (or lack thereof) may also play a role.

B. Offset Ring and Plug

The discontinuities in the ring-and-plug system necessitate the use of higher-order basis functions. The reconstruction for this system is based on 30 wave numbers in both the x direction and the y direction (i.e., $n = m = 30$) and characteristic lengths equal to the sample diameter. Equilibrium is enforced at 1000 equally spaced points. The right-hand sides in Figs. 10 and 11 show the measured

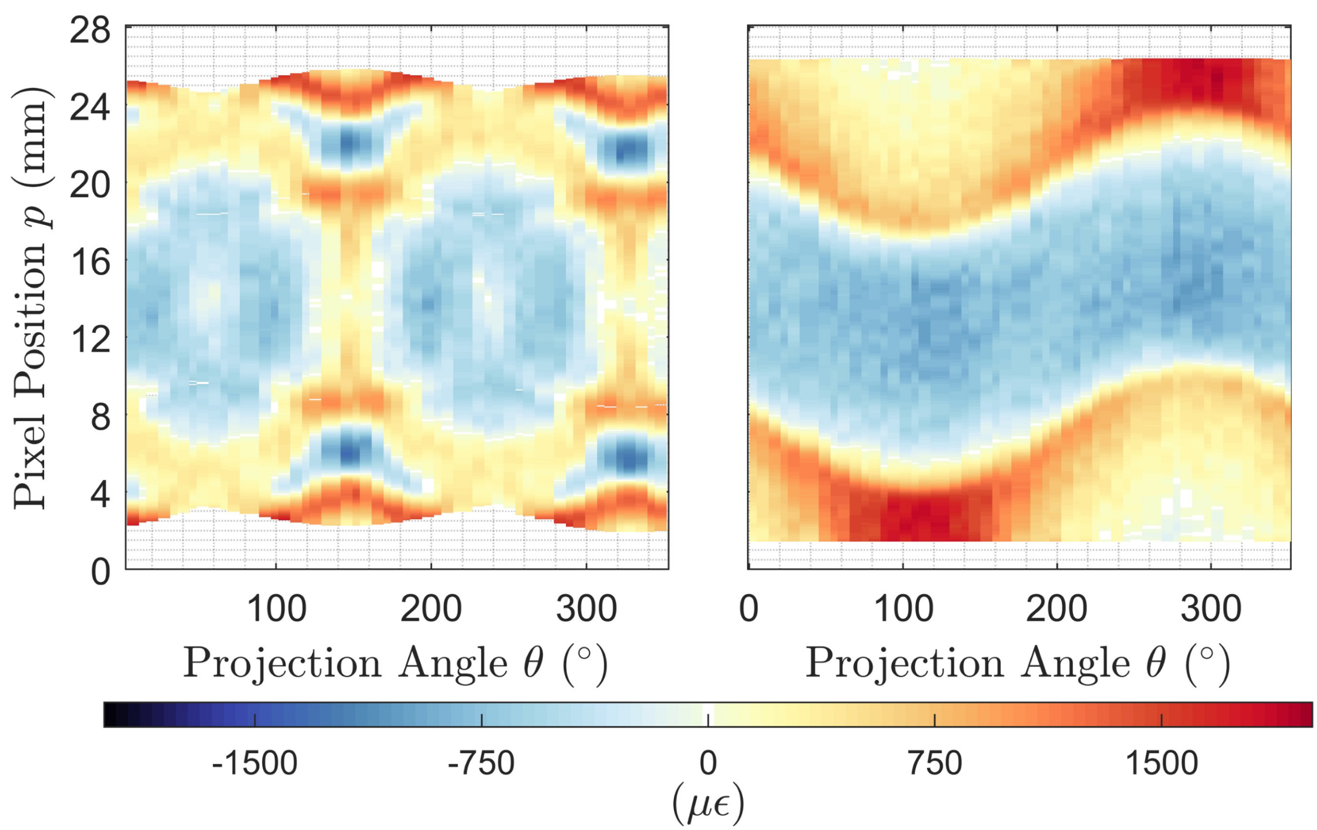

FIG. 10. The measured strain sinograms for the crushed ring and the ring-and-plug system.

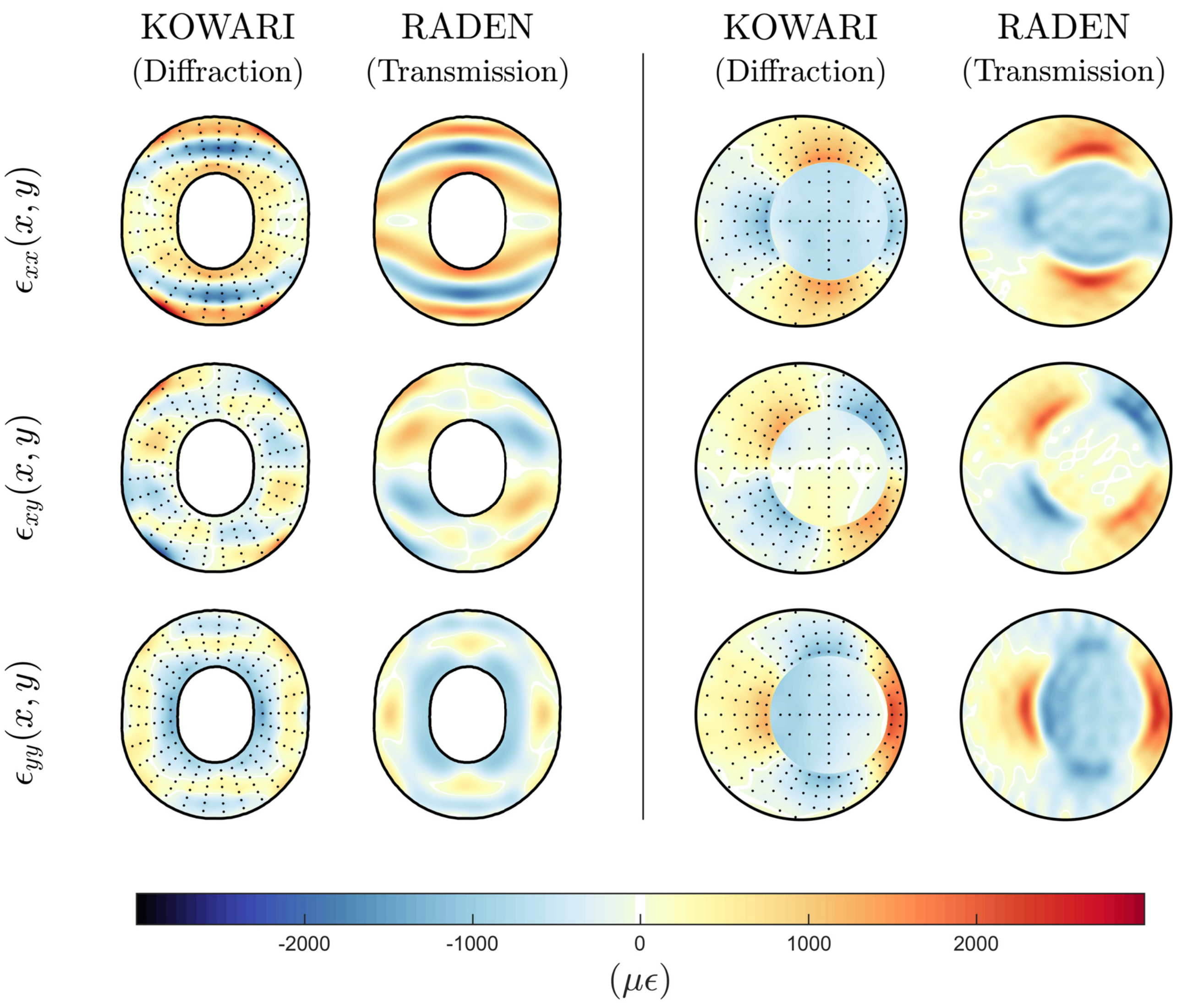

FIG. 11. Strain maps interpolated from pointwise measurements with the KOWARI diffractometer compared to reconstructions from transmission measurements with the RADEN instrument for the crushed ring (left) and the ring-and-plug system (right).

strain sinogram and reconstruction, respectively. Figure 13 shows a comparison over three key cross sections.

As with the crushed ring, the reconstruction and KOWARI measurements show good overall agreement. The discontinuity in strain between the ring and plug obviously presents an interesting challenge, with ringing artifacts clearly present in the reconstruction. This effect is particularly evident in Fig. 13, where overshoots and oscillations can be seen in the region of the step. This effect is lessened by inclusion of higher-order terms, but arbitrarily increasing n and m is not practical; the number of unknown coefficients grows with $12nm$ and can rapidly approach the number of measurements. Before this limit, the computational burden may become impractical.

One potential solution is to use a "tailored" basis in which strains within the ring and plug are constructed from separate basis functions (see, e.g., Ref. [13]). While this can eliminate the ringing, it is not a general approach since it requires prior knowledge of the composition of the system. In effect, the KOWARI measurements we are comparing have been treated in this way; two separate interpolants are used to generate the strain map shown in Fig. 11. This is appropriate in this case given that it serves as a reference with which to compare our reconstruction. It should also be noted that this problem is a direct result of the discontinuity—in the vast majority of practical cases, strain fields tend to be smooth and this issue will not occur.

C. Error assessment

From these results, a quantitative assessment of the discrepancy between the diffraction measurements and tomographic reconstructions is conducted. In both cases, the difference is mean zero and Gaussian. This implies that the

d_0 correction effectively removes the bias associated with sample thickness.

Over the 174 points measured in the crushed ring, the standard deviation of the difference is 370 $\mu\epsilon$. Similarly, over the 195 points measured in the offset ring and plug, the standard deviation is 290 $\mu\epsilon$. These values are slightly higher than expectations based on the simulation results; however, it should be pointed out that we are comparing them with measurements that potentially have their own biases.

VI. EXTENSION TO THREE DIMENSIONS

The algorithm outlined in this paper does not rely on the sample geometry being two-dimensional—in fact it can be easily extended to three dimensions with a small increase in complexity.

In three dimensions there are six unknown components of strain to reconstruct. This obviously increases the computational burden associated with forward mapping and fitting basis functions. For example, a real-valued three-dimensional Fourier series would entail $24n^3$ basis functions for n wave numbers in each direction (as opposed to $12n^2$). However, there is also an additional equation of equilibrium that provides a stronger constraint on any linear combination. The amount of information per projection is also significantly increased (i.e., two-dimensional images versus one-dimensional profiles). From this perspective, the number of projections required is likely to remain roughly equivalent for the same measurement resolution. In three-dimensions, projections would need to be distributed over all directions in three-dimensional space.

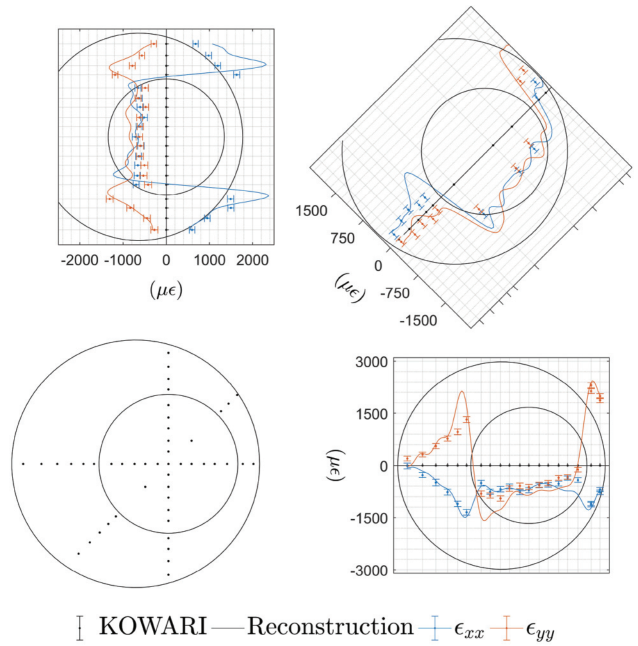

FIG. 13. Distribution of ϵ_{xx} and ϵ_{yy} strain components over a number of cross sections in the ring and plug.

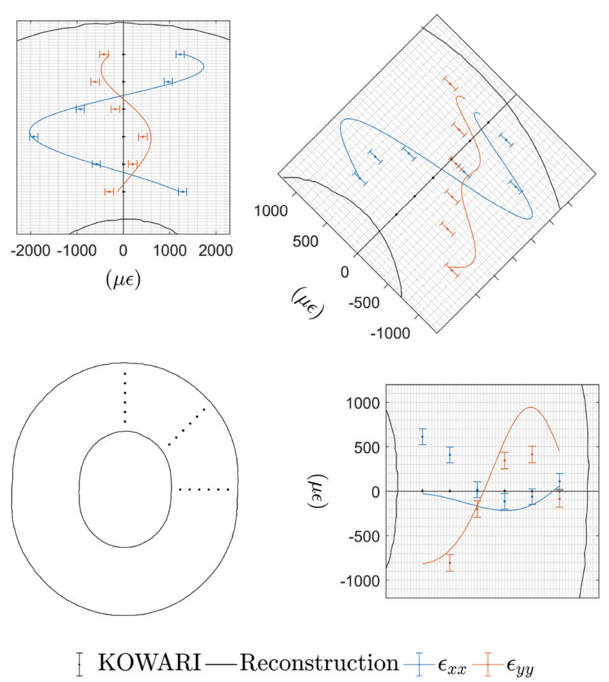

FIG. 12. Distribution of ϵ_{xx} and ϵ_{yy} strain components over a number of cross sections in the crushed ring.

Overall, the size of the problem would be larger but the numerical approach would remain the same.

The true difficulty surrounds the implementation. In three dimensions, correspondingly longer sampling times are required to provide equivalent measurement uncertainty in two-dimensional images. At present this would certainly require compromise in terms of the trade-off between measurement uncertainty and resolution through grouping multiple detector pixels.

In the present work, columns of 256 pixels are grouped to provide one-dimensional profiles; to achieve the same uncertainty in a two-dimensional image, blocks of 16×16 detector pixels ($0.88 \times 0.88\ mm^2$) would be required. Note that this rivals the nominal resolution limits practically achievable with current conventional strain scanners (typically on the order of 1 mm^3). This situation will certainly improve in the future as sources develop; for example, J-PARC is expected to reach 800 kW soon, with additional increases to more than 1 MW scheduled. Once commissioned, the European Spallation Source in Sweden promises to be even brighter. At 800 kW, image resolutions as low as $0.5 \times 0.5\ mm^2$ would be achievable with only a doubling of sampling time. In the current work, we have erred on the side of caution in terms of the uncertainty-resolution compromise at the expense of sampling time; comparable results may have been possible with less beamtime.

Given its importance, the effects of the uncertainty-resolution compromise forms a central question that must be investigated before three-dimensional implementation.

Associating each measurement with a defined path through a known three-dimensional sample geometry also poses significant additional complexity. This is coupled with the fact that more than one axis of rotation is required to view the sample from all directions, with blind spots potentially created by the positioning stage.

If achieved, three-dimensional Bragg-edge tomography has the potential to provide information that cannot practically be measured any other way; full-field mapping in three dimensions using current neutron strain scanners is a difficult process restricted by practical limitations in gauge volume size and count times.

In principle, the issues involved in three-dimensional strain tomography are not insurmountable and they form a natural focus for future work.

VII. CONCLUSION

An algorithm for the reconstruction of biaxial elastic strain tensor fields from Bragg-edge neutron images is presented. In contrast to previous algorithms, our method is capable of reconstructing residual strain since no assumption of elastic strain compatibility is made.

This approach is demonstrated in simulation and with experimental data collected from two samples with the RADEN energy-resolved-neutron-imaging instrument. The results show excellent agreement with strain maps measured with the KOWARI constant-wavelength engineering diffractometer.

While Lionheart and Withers [9] clearly demonstrated that Bragg-edge strain tomography is an ill-posed inverse problem, we achieve the task by considering the physical constraint imposed by equilibrium. This experiment now represents the first-ever tomographic reconstruction of residual strain fields outside simple axisymmetric systems from Bragg-edge data.

At least in two dimensions, full-field Bragg-edge strain tomography can now provide a complementary approach to established pointwise diffraction-based strain-measurement techniques.

The experiment has also highlighted a number of future areas of investigation. These include the effects of beam hardening and strain gradients on the perceived elastic strain inferred from Bragg edges and the extension of the tomographic approach to three-dimensional strain fields.

ACKNOWLEDGMENTS

This work was supported by the Australian Research Council through a Discovery Project Grant No. DP170102324. Access to the RADEN and KOWARI instruments was made possible through the respective user-access programs of J-PARC and ANSTO (J-PARC Long Term Proposal No. 2017L0101 and ANSTO Program Proposal No. PP6050). The authors would also like to thank AINSE Limited for providing nancial assistance (PGRA) and support to enable work on this project.

[1] J. R. Santisteban, L. Edwards, M. E. Fitzpatrick, A. Steuwer, P. J. Withers, M. R. Daymond, M. W. Johnson, N. Rhodes, and E. M. Schooneveld, Strain imaging by Bragg edge neutron transmission, Nucl. Instrum. Methods Phys. Res. Sect. A **481**, 765 (2002).

[2] A. S. Tremsin, J. B. McPhate, A. Steuwer, W. Kockelmann, A. M. Paradowska, J. F. Kelleher, J. V. Vallerga, O. H. W. Siegmund, and W. B. Feller, High-resolution strain mapping through time-of-flight neutron transmission diffraction with a microchannel plate neutron counting detector, Strain **48**, 296 (2012).

[3] A. S. Tremsin, J. B. McPhate, W. Kockelmann, J. V. Vallerga, O. H. W. Siegmund, and W. B. Feller, High resolution Bragg edge transmission spectroscopy at pulsed neutron sources: Proof of principle experiments with a neutron counting MCP detector, Nucl. Instrum. Methods Phys. Res. Sect. A **633**, 235 (2011).

[4] Robin Woracek, Javier Santisteban, Anna Fedrigo, and Markus Strobl, Diffraction in neutron imaging – a review, Nucl. Instrum. Methods Phys. Res. Sect. A **878**, 141 (2018).

[5] J. R. Santisteban, L. Edwards, M. E. Fizpatrick, A. Steuwer, and P. J. Withers, Engineering applications of Bragg-edge neutron transmission, Appl. Phys. A **74**, 1433 (2002).

[6] Brian Abbey, Shu Yan Zhang, Wim J. J. Vorster, and Alexander M. Korsunsky, Feasibility study of neutron strain tomography, Proc. Eng. **1**, 185 (2009).

[7] Brian Abbey, Shu Yan Zhang, Wim Vorster, and Alexander M. Korsunsky, Reconstruction of axisymmetric strain distributions via neutron strain tomography, Nucl. Instrum. Methods Phys. Res. Sect. B **270**, 28 (2012).

[8] Henry J. Kirkwood, Shu Yan Zhang, Anton S. Tremsin, Alexander M. Korsunsky, Nikolaos Baimpas, and Brian Abbey, Neutron strain tomography using the Radon transform, Mater. Today Proc. **2**, 414 (2015).

[9] William R. B. Lionheart and Philip J. Withers, Diffraction tomography of strain, Inverse. Probl. **31**, 045005 (2015).

[10] C. M. Wensrich, J. N. Hendriks, and M. H. Meylan, Bragg edge neutron transmission strain tomography in granular systems, Strain **52**, 80 (2016).

[11] C. M. Wensrich, J. N. Hendriks, A. Gregg, M. H. Meylan, V. Luzin, and A. S. Tremsin, Bragg-edge neutron transmission strain tomography for in situ loadings, Nucl. Instrum. Methods Phys. Res. B **383**, 52 (2016).

[12] J. N. Hendriks, A. W. T. Gregg, C. M. Wensrich, A. S. Tremsin, T. Shinohara, M. Meylan, E. H. Kisi, V. Luzin, and O. Kirsten, Bragg-edge elastic strain tomography for in situ systems from energy-resolved neutron transmission imaging, Phys. Rev. Mater. **1**, 053802 (2017).

[13] A. W. T. Gregg, J. N. Hendriks, C. M. Wensrich, and M. H. Meylan, Tomographic reconstruction of residual strain in axisymmetric systems from bragg-edge neutron imaging, Mech. Res. Commun. **85**, 96 (2017).

[14] C. Jidling, J. Hendriks, N. Wahlstrom, A. Gregg, T. B. Schon, C. Wensrich, and A. Wills, Probabilistic modelling and reconstruction of strain, Nucl. Instrum. Methods Phys. Res. B **436**, 141 (2018).

[15] C. E. Rasmussen and C. K. I. Williams, *Gaussian Processes for Machine Learning*, Adaptive Computation and Machine Learning (MIT Press, Cambridge, MA, USA, 2006), p. 248.

[16] F. P. Beer, E. R. Johnston, Jr., J. T. DeWolf, and D. F. Mazurek, *Mechanics of Materials* (McGraw-Hill, 2008).

[17] T. Shinohara, T. Kai, K. Oikawa, M. Segawa, M. Harada, T. Nakatani, M. Ooi, K. Aizawa, H Sato, T. Kamiyama *et al.*, in *Journal of Physics: Conference Series* (IOP Publishing, 2016), Vol. 746, p. 012007.

[18] Takenao Shinohara and Tetsuya Kai, Commissioning start of energy-resolved neutron imaging system, RADEN in J-PARC, Neutron News **26**, 11 (2015).

[19] Sven Vogel, PhD thesis, Christian-Albrechts Universität Kiel, 2000.

[20] R. A. Brooks and G. Di Chiro, Beam hardening in x-ray reconstructive tomography, Phys. Med. Biol. **21**, 390 (1976).

[21] J. Huang, S. C. Vogel, W. J. Poole, M. Militzer, and P. Jacques, The study of low-temperature austenite decomposition in a fecmnsi steel using the neutron bragg edge transmission technique, Acta Mater. **55**, 2683 (2007).

[22] S. Vogel, E. Ustundag, J. C Hanan, V. W. Yuan, and M. A. M. Bourke, In-situ investigation of the reduction of NiO by a neutron transmission method, Mater. Sci. Eng.: A **333**, 1 (2002).

[23] H. Sato, T. Kamiyama, and Y. Kiyanagi, A rietveld-type analysis code for pulsed neutron bragg-edge transmission imaging and quantitative evaluation of texture and microstructure of a welded α-iron plate, Mater. Trans. **52**, 1294 (2011).

[24] H. Sato, T. Shinohara, R. Kiyanagi, K. Aizawa, M. Ooi, M. Harada, K. Oikawa, F. Maekawa, K. Iwase, and T. Kamiyama *et al.*, Upgrade of bragg edge analysis techniques of the rits code for crystalline structural information imaging, Phys. Proc. **43**, 186 (2013).

[25] H. Sato, K. Watanabe, K. Kiyokawa, R. Kiyanagi, K. Y. Hara, T. Kamiyama, M. Furusaka, T. Shinohara, and Y. Kiyanagi, Further improvement of the rits code for pulsed neutron bragg-edge transmission imaging, Phys. Proc. **88**, 322 (2017).

[26] Li Feng, Robert Grimm, Kai Tobias Block, Hersh Chandarana, Sungheon Kim, Jian Xu, Leon Axel, Daniel K. Sodickson, and Ricardo Otazo, Golden-angle radial sparse parallel MRI: Combination of compressed sensing, parallel imaging, and golden-angle radial sampling for fast and flexible dynamic volumetric MRI, Magn. Reson. Med. **72**, 707 (2014).

[27] Erich H. Kisi and Christopher J. Howard, *Applications of Neutron Powder Diffraction* (Oxford University Press, New York, 2012), Vol. 15.

[28] Michael E. Fitzpatrick and Alain Lodini, *Analysis of Residual Stress by Diffraction using Neutron and Synchrotron Radiation* (CRC Press, Boca Raton, 2003).

[29] Ismail C. Noyan and Jerome B. Cohen, *Residual stress: Measurement by Diffraction and Interpretation* (Springer, New York, 2013).

[30] O. Kirstein, V. Luzin, and U. Garbe, The strain-scanning diffractometer KOWARI, Neutron News **20**, 34 (2009).

[31] Alain Brule and Oliver Kirstein, Residual stress diffractometer KOWARI at the Australian research reactor OPAL: Status of the project, Phys. B: Condens. Matter **385**, 1040 (2006).

[32] Oliver Kirstein, Ulf Garbe, and Vladimir Luzin, in *Materials Science Forum* (Trans Tech Publications, Switzerland, 2010), Vol. 652, p. 86.

[33] M. R. Daymond and H. G. Priesmeyer, Elastoplastic deformation of ferritic steel and cementite studied by neutron diffraction and self-consistent modelling, Acta Mater. **50**, 1613 (2002).